Quantifying Dispersion of Nanoparticles in Polymer Nanocomposites Through TEM Micrographs

Xiaodong Li[1*], Hui Zhang[2], Jionghua Jin[3], Dawei Huang[4], Xiaoying Qi[2], Zhong Zhang[2] and Dan Yu[1]

1. NCMIS, Academy of Mathematics and Systems Science, Chinese Academy of Sciences, Beijing, China.
2. National Center for Nanoscience and Technology, Beijing, China.
3. Department of Industrial and Operations Engineering, University of Michigan, MI, U.S.A.
4. Academy of Mathematics and Systems Science, Chinese Academy of Sciences, Beijing, China.

*corresponding author: xli@amss.ac.cn

Abstract

The property of nanocomposites is crucially affected by nanoparticle dispersion. Transmission Electron Microscopy (TEM) is the "golden standard" in nanoparticle dispersion characterization. A TEM Micrograph is a 2-dimensional (2D) projection of a 3-dimentional (3D) ultra-thin specimen (50~100 nanometers thick) along the optic axis. Existing dispersion quantification methods assume complete spatial randomness (CSR), or equivalently the homogeneous Poisson process as the distribution of the centroids of nanoparticles under which nanoparticles are randomly distributed. Under the CSR assumption, absolute magnitudes of dispersion quantification metrics are used to compare the dispersion quality across samples. However, as hard nanoparticles do not overlap in 3D, centroids of nanoparticles cannot be completely randomly distributed. In this paper, we propose to use the projection of the exact 3D hardcore process, instead of assuming CSR in 2D, to firstly account for the projection effect of a hardcore process in TEM micrographs. By employing the exact 3D hardcore process, the thickness of the ultra-thin specimen, overlooked in

previous research, is identified as an important factor that quantifies how far the assumption of Poisson process in 2D deviates from the projection of a hardcore process. The paper shows that the Poisson process can only be seen as the limit of the hardcore process as the specimen thickness tends to infinity. As a result, blindly using the Poisson process with limited specimen thickness may generate misleading results. Moreover, because the specimen thickness is difficult to be accurately measured, the paper also provides robust analysis of various dispersion metrics to the error of claimed specimen thickness. It is found that the quadrat skewness and the K-function are relatively more robust to the misspecification of the specimen thickness than other metrics. Furthermore, analysis of detection power against various clustering degrees is also conducted for these two selected robust dispersion metrics. We find that dispersion metrics based on the K-function is relatively more powerful than the quadrat skewness. Finally, an application to real TEM micrographs is used to illustrate the implementation procedures and the effectiveness of the method.

Keywords: Nanoparticle Dispersion, Transmission Electron Microscopy, Poisson Process, Hardcore Process

1 Introduction

In recent years, polymer nanocomposites have attracted great interest in both nanomaterial research and industrial application [1-3]. Nanoparticles, in comparison with microparticles, have been found to offer polymers better mechanical, electrical and optical performance, etc. Homogeneous and aggregate-free dispersion of nanoparticles in the polymer matrix is essential for the manufacturing of nanocomposites, so as to realize their superior performance [4-5]. However, due to their small dimensions and high specific surface

areas, nanoparticles are easy to stick to each other and form micron-sized aggregates. At poor dispersion level of nanoparticles, the performance of nanocomposites degrades significantly and sometimes is even worse than that of microcomposites. In mechanics, large aggregates cause stress concentrations around them and induce pre-mature fracture of composite materials [6-9]. In electrical transmission industry, large aggregates may act as defects that induce partial discharge and early breakdown [10]. In optics, large aggregates can interfere with light propagation, thus decrease the transparency and increase the haze of nanocoatings [11].

In the manufacturing process of nanocomposites, there are usually a number of factors that can affect the dispersion of nanoparticles and further the properties of nanocomposites. It is of great interest to learn how these factors may be selected so as to optimize the manufacturing process and in the end lead to an efficient process control procedure. Nanoparticle dispersion is intrinsically linked with both the process variables and the resulting properties of the nanocomposite. Moreover, since some tests on nanocomposite properties (e.g. fretting resistance) may be destructive, assessing nanoparticle dispersion may provide an effective surrogate for process optimization and control.

Currently, nanoparticle dispersion is mostly evaluated by qualitatively interpreting micrographs taken from transmission electron microscopy (TEM) [12]. Because qualitative evaluation of TEM micrographs is subjective and may differ largely from one inspector to another, it cannot meet the demands for large-scale manufacturing processes in which an automatic quantification measure of nanoparticle dispersion is required. As a result, effective quantitative measures of nanoparticle dispersion through TEM micrographs are the

prerequisite for the mass production of nanocomposites.

To perform TEM measurements, the sample material is first prepared into an ultra-thin specimen before placed onto the mesh copper grids for imaging (shown in Fig. 1a). The thickness of the ultra-thin specimen is approximately from 50 to 100 nanometers (nm), usually several times of the size of commonly used nanoparticles. The obtained image is a two dimensional (2D) projection (shown in Fig. 1b) of the three dimensional (3D) specimen along the optic axis (axis z in Fig. 1a) [13].

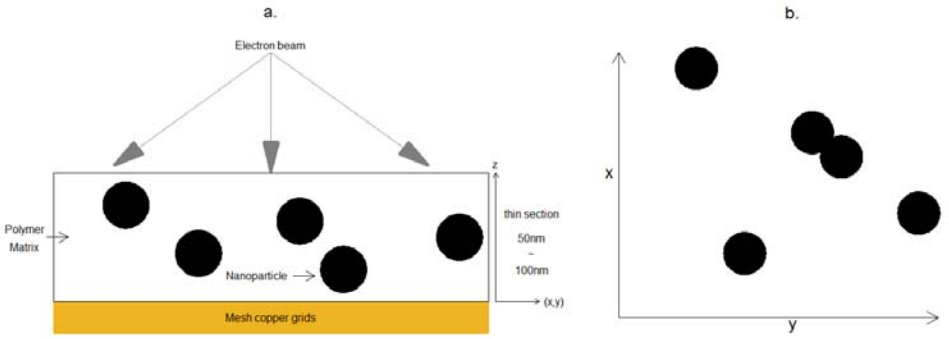

Figure 1. Illustration of the projection view of TEM micrographs.

A key question to nanoparticle dispersion quantification is whether the nanoparticles form clusters in the material, and if yes how severe the clustering is. A number of methods have been proposed to achieve this goal. These methods generally fall into two categories. The first category assumes each nanoparticle as a point (e.g., the centroid of a nanoparticle) on the 2D micrograph and studies the distribution of all the points. It is directly related to the analysis of 2D spatial point patterns, which have been extensively studied in areas such as ecology, biology and astronomy [14-16]. For example, dispersion metrics based on quadrat counts and spatial distances have been used as direct quantifiers for the degree of nanoparticle dispersion [17-19]. Algorithms based on the Dirichlet tessellation [20, 21] and the rotating axis [22] have also been shown to be effective in distinguishing clustering point

patterns. The complete spatial randomness (CSR) or equivalently the homogeneous Poisson process has long been used as the "standard" model for 2D spatial point patterns [14]. It assumes that the number of points falling into any region follows a poisson distribution with an expectation proportional to the area of the region. It also assumes that the numbers of points falling into two disjoint regions are independent from each other. In particular, given a fixed number of n points, the n points are independent and uniformly distributed. Under the null hypothesis of CSR, the aforementioned methods have been compared with respect to their detection power for clustering [23]. The second category mainly focuses on the unreinforced domains of polymers, i.e., the space free of nanoparticles. Proposed dispersion metrics include the mean inter-particle distance [24-26], a measure of the deviation from the mean inter-particle distance, called the "free-path spacing" [27] and the length of the largest area for which the mode of particle number is zero, called the "free-path length" [28]. Another interesting idea is to use the expansion pattern of nanoparticles on the binarized image of the TEM micrograph to differentiate different specimens [29].

In general, dispersion metrics can be used either as test statistics for a statistical test of clustering or as direct quantifiers for the degree of clustering to compare different samples. Existing methods employ 2D CSR as the "standard" model of random nanoparticle distribution [23, 27]. In addition, sample comparison is based on the absolute magnitudes of dispersion metrics. These approaches are valid only if CSR is the correct "standard" model and the "standard" models for different samples can be assumed to be the same. In reality, a TEM micrograph should be considered as a 2D projection of the 3D ultra-thin specimen, so the "standard" model should actually originate from a 3D random distribution and then

project onto 2D. If the distribution for centroids of nanoparticles were CSR in 3D, the use of CSR would be valid. However, as most nanofillers are hard particles that cannot overlap in 3D, the centroids of nanoparticles cannot be completely random in 3D, i.e., they are subject to constraints. As an example, for spherical nanoparticles, the constraint in 3D is equivalent to set the minimum distance between the centroids of any two nanoparticles to be equal to the sum of their radiuses. This type of model is named as the "hardcore" process in spatial statistics. To our knowledge, there is little investigation on how the behavior of dispersion metrics is affected by employing the projection of a 3D hardcore process as the "standard" model. Although the concept of a random hardcore model has been used to construct a dispersion metric based on the Delaunay network [30], the hardcore constraint was put on the 2D micrographs rather than on the exact 3D distribution of nanoparticles. Apparently, under the 3D hardcore model, aggregates with multiple particles can be observed in 2D although these particles do not overlap at all in 3D (shown in Fig. 1a and 1b).

The hardcore process exhibits more regular patterns than the Poisson process. In addition, unlike the Poisson process, the distribution of the 2D projection of a 3D hardcore process may depend on the thickness of the thin specimen under imaging. The effect of thickness needs to be incorporated for more accurate inferences, which, however, is ignored in the existing methods. This paper attempts to explore the possible gap between the currently available dispersion quantification methods and the proposed method to consider the exact projection of 3D hardcore process.

Another question arises whether 2D TEM micrograph can represent the dispersion of 3D materials. Attempts have been made to relate TEM observations to 3D dispersion

parameters through stereology analysis [25, 31]. However, length is considered as an observation from a cross-sectional plane of the 3D material and the projection effect of TEM micrographs is completely ignored. This negligence may severely impact the stereological relationships between nanoparticles if the thickness of the thin specimen is comparable to the size of nanoparticles [32]. In this paper, the representativeness of 2D TEM micrographs for 3D thin specimens is also investigated through simulations.

To limit the scope of this paper, we focus on the distribution behaviors of centroids of nanoparticles or aggregates. To investigate representatives of 2D dispersion measures for 3D dispersion, we will mainly discuss the commonly used quadrat-based methods and the distance-based methods. In addition, the number of nanoparticles/aggregates, closely related to the 'TEM dispersion' [33] will also be investigated.

The rest of the paper is organized as follows. In Section 2, the hardcore process in 3D is introduced as the "standard" model for nanoparticle dispersion in 3D, which is compared with the current practice using a Poisson process. In Section 3, the detailed characteristic analysis of dispersion metrics under the hardcore process is provided through simulations. Specifically, the dispersion metrics to be investigated are introduced first, and then the selection of robust dispersion metrics insensitive to the claimed thickness of the specimen is discussed. Afterwards, power analysis is conducted to compare those selected robust dispersion metrics. In Section 4, real TEM micrographs are analyzed to demonstrate the implementation procedures and the effectiveness of the proposed methods. Finally, we conclude the paper in Section 5.

2 Basis of the Proposed Hardcore Process

The projection of a 3D hardcore process onto 2D reflects both the working principle of TEM and the practical distributional constraints of hard nanoparticles, so it is proposed as the "standard" model for nanoparticle dispersion in a TEM micrograph. In this paper, we focus on a simple scenario, in which nanoparticles are uniform-size spheres in 3D and their diameters are smaller than the thickness of the thin specimen. Then the hardcore constraint is equivalent to that the distance between the centroids of any two nanoparticles cannot exceed the diameter of a nanoparticle.

Let *l*, *w* and *h* denote the length, width and thickness of the field of view for the TEM micrograph and $\mathcal{H} = [0, w] \times [0, l] \times [0, h]$ denote the 3D imaging region. Let *r* denote the radius for a nanoparticle and $\boldsymbol{x} = \{\boldsymbol{x_1}, \dots, \boldsymbol{x_n}\}$ with $\boldsymbol{x_i} = (x_{i1}, x_{i2}, x_{i3}) \in \mathcal{H}$ represent centroids of *n* nanoparticles. Then the probability density for a 3D hardcore process $\boldsymbol{x}$ can be written as:

$$f(\boldsymbol{x}) = \begin{cases} \dfrac{1}{\alpha * (wlh)}, if \left\|\boldsymbol{x_i} - \boldsymbol{x_j}\right\| > 2r \quad \forall i \neq j \\ 0 \qquad\qquad\qquad\qquad\qquad\qquad \text{otherwise} \end{cases}$$

where $\|u - v\|$denotes the 3D Euclidean distance between *u* and *v* and α is the normalizing constant to make the integration of $f(\boldsymbol{x})$ over $\mathcal{H}$ equal to one. A Poisson process with *n* points in $\mathcal{H}$ is simply a uniform distribution in $\mathcal{H}$. So the intensity of the hardcore process is equivalent to that of the Poisson process conditioned on the event that no two points lie closer than $2r$ units apart. Then α has a probabilistic meaning $1 - \alpha = \mathrm{P}\left(\cup_{1 \le i \neq j \le n} A_{ij}\right)$, where $A_{ij} = \left\{\left\|\boldsymbol{x_i} - \boldsymbol{x_j}\right\| \le 2r\right\}$ with $\boldsymbol{x_i}$ and $\boldsymbol{x_j}$ uniformly distributed in $\mathcal{H}$. The closer α is to one, the more similar the hardcore process is to the Poisson process in 3D. Generally, α is not in tractable forms. The upper and lower bounds for α can be derived and are given in Proposition 1. The proof of Proposition 1 can be found in the Appendix.

Proposition1. For any *n* and *w, l, h>4r, the following inequalities hold:*

$$\eta_L \le 1-\alpha \le \eta_U$$

$$\eta_L = \max\{s_1(n)\frac{\pi r^3}{wlh} - s_2(n)(\frac{\pi r^3}{wlh})^2, 0\},$$

$$\eta_U = \min\{t_1(n)\frac{\pi r^3}{wlh} - t_2(n)(\frac{\pi r^3}{wlh})^2 + t_3(n)\,(\frac{\pi r^3}{wlh})^3, 1\},$$

where the detailed forms of $s_1(n), s_2(n), t_1(n), t_2(n)$ *and* $t_3(n)$ *are in the appendix.*

The distinction of the hardcore process from the Poisson process is governed by all of its parameters. But some of these parameters can be considered known *a priori* for a TEM experiment. For example, the micrograph size *w* and *l* can be determined from the magnification factor when taking the TEM micrograph; the radius *r* can usually be obtained from the source information of the raw material. As a result, the number of nanoparticles *n* and the thickness of the thin specimen *h* are two key parameters that affect how far away a Poisson process deviates from the hardcore process. This result can help judge the application region beyond which the existing dispersion quantification methods using the Poisson process model may fail.

Table 1 provides the bounds calculated from Proportion 1 for varying *h* and *n* when other parameters are set the same as the real TEM micrographs studied in Section 4 (*w*=*l*=1067nm and 2*r*=21nm). Two different numbers of nanoparticles *n* under evaluation are set as n_1 =423 and n_2 =1409, which correspond to the expected number of nanoparticles whose centroids follow the hardcore process under a specimen thickness of 60nm, for a content of nanoparticles at 3% or 10% respectively. These settings for the number of particles are also investigated in the simulation study in Section 3. For a fixed *n*, the lower and upper

bounds approach each other when h increases to a much larger magnitude than the radius r of nanoparticles. Under the extreme case, when h goes to infinity and n is fixed, α approaches one. As a result, if h is large enough, there is little difference between the hardcore process and the Poisson process. In case of a fixed h, increasing n results in a fast decrease of α. Therefore, in order for a hardcore process to converge to the Poisson process, a larger h is required with increasing n.

Table 1. The lower and upper bounds for α.

$h(\mu m)$	n_1=423			n_2=1409		
	lower	upper	simulated	lower	upper	simulated
10	0.74	0.75	0.75	0	1	0.04
100	0.97	0.97	0.97	0.72	0.72	0.72
1000	1	1	1	0.97	0.97	0.97
10000	1	1	1	1	1	1

In practice, the number of nanoparticles n can be obtained through image processing techniques, which will be discussed in Section 4. So, n can also be pragmatically fixed for a given TEM micrograph. In this case, h is the only parameter that affects how far away a Poisson process deviates from the hardcore process. As a direct application of Proposition 1, the following proposition can be obtained.

Proposition 2. For fixed w, l, r and n, the hardcore process in $\mathcal{H}$ converges to the Poisson process in $\mathcal{H}$ as $h\rightarrow \infty$. As a result, the projection of the hardcore process in $\mathcal{H}$ onto $W = [0, l] \times [0, w]$ converges to a Poisson process in W as $h\rightarrow \infty$.

The interpretation of Proposition 2 is intuitive. When h goes to infinity with all the other parameters fixed, the randomly distributed nanoparticles tend to be highly dispersed in space, and therefore the hardcore constraint does not play a role anymore. Proposition 2 provides an intrinsic relationship between the projection of the 3D hardcore process and the

Poisson process in 2D. In fact, the Poisson process can be seen as a projected hardcore process with infinite thickness. In practice, the thickness of the thin specimen under TEM imaging is rarely larger than 100nm, much smaller than the required h for the hardcore process to converge to the Poisson process. Therefore, blindly using the Poisson process for hypothesis testing or dispersion quantification may generate misleading results. In addition, Proposition 2 also indicates that the thickness h of the thin specimen is an important factor in judging whether a Poisson process can be approximately used. The impact of varying h on the distribution of dispersion metrics under the projected hardcore process will be studied extensively through simulations in Section 3.2. The simulation of the hardcore process in 3D can be conveniently done via Markov Chain Monte Carlo simulation algorithms [34].

3 Characteristic Analysis of the Dispersion Metrics

Dispersion metrics based on spatial statistics have been studied extensively under the Poisson process. However, their characteristics under the proposed hardcore process are still elusive. We analyze them in this section. In Section 3.1, the related dispersion metrics under consideration in this paper are introduced. In Section 3.2, following the conclusion in Proposition 2, the impact of the specimen thickness h on the use of dispersion metrics is investigated through simulations, based on which the robust dispersion metrics insensitive to the misspecification of h are selected. In Section 3.3, we further evaluate the performance of those selected robust dispersion metrics on detecting clustering patterns through simulations.

3.1 Dispersion Metrics to be Studied

Two most commonly used types of dispersion metrics, which are based on spatial

statistics and the number of aggregates, are selected to be evaluated under the projected hardcore process. Detailed definitions of those dispersion metrics as well as their applicability are provided in Table 2. The quadrat-based and the distance-based metrics can be applied to point patterns generated from the centroids of 3D nanoparticles, and the centroids of either nanoparticles or aggregates projected in 2D. Since nanoparticles do not overlap and thus do not form aggregates in 3D, the dispersion metric based on the number of aggregates can only be calculated based on the projected nanoparticles in 2D.

The quadrat-based and the number-of-aggregates-based dispersion metrics are explicit summary statistics of nanoparticle dispersion, so they may be directly used to quantify nanoparticle dispersion or serve as test statistics for hypothesis testing. The distance-based methods provide function summaries of dispersion, i.e., an estimated curve instead of a single number for each micrograph. Thus the corresponding one-dimensional summary statistic has to be provided based on some distance metric to a reference curve. In this paper, the integrated squared error of the estimated curve from the null hypothesis curve under a projected hardcore process is used. This is a two-sided test statistic, i.e., it does not differentiate between point patterns that are more regular or more clustered than the projected hardcore process. For the K and G functions, a higher value than the reference suggests clustering, while for the F function, a lower value than the reference suggests clustering. So, a one-sided test statistic T_2 is also considered.

Table 2. Definitions and applicability of dispersion metrics.

Quadrat-based methods: 3D or 2D particle-based and 2D aggregate-based
● Index of dispersion (ID): ID $= (k-1)s^2/\bar{z}$ ● Shannon entropy (SE): SE $= -\sum_{i=1}^{k} p_i \log(p_i)$

• Skewness (SK): $\mathrm{SK} = \frac{k}{(k-1)(k-2)} \sum_{i=1}^{k} \left(\frac{z_i - \bar{z}}{s}\right)^3$ k: the number of quadrats; z_i: the number of points in the i-th quadrat; $\bar{z} = \sum_{i=1}^{k} z_i/k$; $s = \sqrt{\sum_{i=1}^{k}(z_i - \bar{z})^2/(k-1)}$; $p_i = z_i / \sum_{l=1}^{k} z_l$.
Distance-based methods: 3D or 2D particle-based and 2D aggregate-based
• K function: $\mathrm{K}(t) = \frac{1}{\lambda}\mathrm{E}[n(\boldsymbol{x} \cap b(u,t) \backslash \{u\}) \mid u \in \boldsymbol{x}]$ • F function: $\mathrm{F}(t) = \mathrm{P}(b(u, \boldsymbol{x}) \leq t)$ • G function: $\mathrm{G}(t) = \mathrm{P}(b(u, \boldsymbol{x} \backslash \{u\}) \leq t \mid u \in \boldsymbol{x})$ λ: the intensity of the point process; $\boldsymbol{x}$: the point process; $b(u,t) = \{v: \|u - v\| \leq t\}$; $b(u, \boldsymbol{x}) = \mathrm{argmin}_{v \in \boldsymbol{x}} \|u - v\|$; $\boldsymbol{x} \backslash \{u\}$: the point process $\boldsymbol{x}$ excluding u. $T_1 = \int [\widehat{H}(t) - H(t)]^2 dt$; $T_2 = \int_{D(t)} \left[\widehat{H}(t) - H(t)\right]^2 dt$, where $\widehat{H}(t)$ denotes the estimated K, F or G function and $H(t)$ denotes the reference function; $D(t) = \{\widehat{H}(t) \geq H(t)\}$ for the K and G functions and $D(t) = \{\widehat{H}(t) < H(t)\}$ for the F function.
TEM dispersion: 2D particle-based
• Number of aggregates ($\mathrm{N_{n/a}}$): $\mathrm{N_{n/a}} = \#\{Y_i : d(Y_i, Y_i) < 2r, d(Y_i, Y_j) \geq 2r, i \neq j\}$, where $\{Y_1, \ldots, Y_{\mathrm{N_{n/a}}}\}$ forms a partition for a 2D point process $\{y_1, \ldots, y_n\} \in W$; $d(Y_i, Y_i) = \max_{u \in Y_i} d(u, Y_i)$, where $d(u, Y_i) = \min_{v \in Y_i} \|u - v\|$; $d(Y_i, Y_j) = \min_{u \in Y_i} d(u, Y_j)$.

Although all the above metrics can quantify the dispersion of nanoparticles to some degrees, there is no consensus on the choice of the metrics for real applications, even under the Poisson process assumption. In the following two subsections 3.2 and 3.3, we shall systematically investigate the robustness of these metrics under a certain misspecification of the thin specimen thickness and their detection power against clustering, respectively.

3.2 Robustness of the Dispersion Metrics

For a TEM experiment with a fixed magnification factor level and a fixed size of

nanoparticles, the remaining two parameters affecting 2D projection of the hardcore process are the number of nanoparticles and the specimen thickness. The particle number information can usually be obtained from image processing, but the exact thickness *h* is usually hard to obtain. Usually, rough thickness estimation can be obtained by using the thickness control parameter during TEM sample preparation using ultramicrotome. However, the tolerance in error can be in tens of nanometers. An illustrative example for the potential impact of *h* on the distribution of dispersion metrics is shown in Fig. 2.

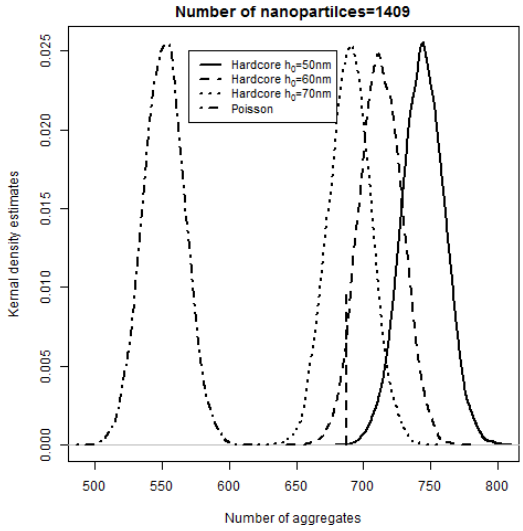

Figure 2. Illustrative example of the impact of *h* on dispersion metrics.

For w=l=1067nm, r=10.5nm and a fixed number of n=1409 nanoparticles, the projected hardcore process with a true specimen thickness h_0 of 50nm (solid), 60nm (dash), and 70nm (dot) as well as the Poisson process (dot and dash) are simulated. The probability density functions (PDF) for the number of aggregates under the above four processes are estimated from 10000 replicated simulations for each process using kernel density estimates and are plotted in Fig. 2. It is seen that the PDF under the Poisson process is almost

completely separated from the PDF under a projected hardcore process with a limited h_0. Even when the specimen thickness is not very different from one another (50nm to 70nm), the PDFs still shift dramatically. This phenomenon implies that h makes a substantial impact on the use of the number of aggregates as a test statistic or as a direct dispersion quantifier. For example, assume that a number of 687 aggregates (indicated by the dashed vertical line in Fig. 2) are observed on a TEM micrograph, which corresponds to the 5th percentile of the dashed PDF with $h_0 = 60\text{nm}$. If the claimed thickness of specimen is 50nm, the dashed vertical line is far to the left tail of the solid PDF with $h_0 = 50\text{nm}$. This misleadingly indicates more severe clustering for the specimen with a claimed thickness of 50nm than that of 60nm. On the contrary, for the specimen with a claimed thickness of 70nm or being very thick, which is corresponding to the null hypothesis of $h_0 = 70\text{nm}$ or $h_0 = \infty(\text{Poisson})$, the statistical test for clustering yields a higher p-value, thus misleadingly concluding less clustering than under $h_0 = 60\text{nm}$. This example shows that the claimed thickness of a specimen may possibly affect results for statistical testing and sample comparison using dispersion metrics of nanoparticles.

Considering that it is generally difficult to exactly measure the thickness of a specimen, it is desirable to identify some robust dispersion metrics so that their performance are little sensitive to misspecification of specimen thickness. For this purpose, the following simulation studies are conducted to systematically evaluate the potential impact of h on various dispersion metrics based on observations on 2D micrographs. Specifically, the robustness of a dispersion metric is evaluated by comparing its Type I error rate under a claimed specimen thickness h with a nominal Type I error rate of 0.05 under the true

specimen thickness h_0 ($h_0 \neq h$). The detailed simulation conditions/parameters are given below:

- w=l=1067nm; r=10.5nm;
- Number of nanoparticles(n): n_1=423, $n_2 = 1409$;
- True section thickness: $h_0 = 50, 60$ or 70nm;
- Claimed section thickness h=50, 60, 70nm and ∞ (Poisson);
- Number of duplicates for each setting: 10000.

For the quadrat-based metrics, w and l are both equally divided into S (set to be 5, 15 and 25) parts, so the number of quadrats on a micrograph satisfies the condition of k=S×S. For the dispersion metrics SE and $\mathrm{N_{n/a}}$, a smaller value indicates clustering. So their negative numbers are used as the test statistics. For the quadrat-based and the number-of-aggregates-based metrics, Type I error rate can be calculated as $\mathrm{P}(T_{h_0} \geq C_{0.05,h})$, where T_{h_0} denotes the corresponding test statistic under a projected hardcore process with true h_0 and $C_{0.05,h}$ denotes the 95$^{\text{th}}$ percentile of the test statistic under a projected hardcore process with h.

For the distance-based metrics, Type I error rate for the two-sided test can be calculated as $\mathrm{P}(T_{1,h_0,h} \geq C_{0.05,h})$, where $T_{1,h_0,h} = \int\left[\widehat{H}_{h_0}(t) - H_h(t)\right]^2 \mathrm{d}t$ and $C_{0.05,h}$ is the 95$^{\text{th}}$ percentile of $\int\left[\widehat{H}_h(t) - H_h(t)\right]^2 \mathrm{d}t$, where $\widehat{H}_{h_0}(t)$ and $\widehat{H}_h(t)$ denote the estimated function under the hardcore process with a specimen thickness of h_0 and h, respectively. The true function $H_h(t)$ is obtained through averaging the results over 5000 duplicates in the simulation. The one-sided test can be similarly conducted. Type I error rates calculated from the simulations are presented in Tables 3~5 corresponding to quadrat-based, distance-based,

and the number-of-aggregates-based dispersion metrics, respectively.

In Table 3, *S*=5, 15 and 25 are used in the simulations. For *S*=25, the area of each quadrat is approximately 17 and 5 times as large as the average effective particle/aggregate size for $n_1 = 423$ and $n_2 = 1409$, respectively. This quadrat size is smaller than the suggested quadrat size in literature [35]. The reason of not selecting an even larger *S* is its high sensitivity to the claimed specimen thickness, which can be seen from Table 3. The robustness of the dispersion metrics deteriorates when *S* or the number of nanoparticles *n* increases, and when particle centroids instead of aggregate centroids are used. Out of the three quadrat-based metrics, only the skewness metric is robust to the claimed specimen thickness with Type I error rates close to 0.05 under both n_1 and n_2 for both particle-based and aggregate-based pattern at *S*=5 or 15. When *S*=25, the particle-based skewness metric is also sensitive to misspecification of *h* (e.g., Type I error rate is higher than 0.1 in some cases).

Table 3. Type I error rates for quadrat-based methods.

	h_0	h	$n = n_1 = 423$									$n = n_2 = 1409$								
			ID *S*=			SE *S*=			SK *S*=			ID *S*=			SE *S*=			SK *S*=		
			5	15	25	5	15	25	5	15	25	5	15	25	5	15	25	5	15	25
Particle-based	50	70	.03	.02	.01	.03	.02	.01	**.05**	**.03**	.01	.01	0	0	.01	0	0	**.05**	**.03**	.01
		∞	.01	0	0	.01	0	0	.04	0	0	0	0	0	0	0	0	.04	0	0
	60	50	.07	.09	.12	.07	.08	.11	**.05**	**.07**	.09	.1	.21	.33	.1	.19	.3	**.05**	**.07**	.1
		70	.04	.03	.02	.04	.03	.02	**.05**	**.05**	.03	.03	.01	0	.02	.02	.01	**.05**	**.04**	.02
		∞	.01	0	0	.01	0	0	.04	.01	0	0	0	0	0	0	0	.04	0	0
	70	50	.08	.13	.2	.08	.12	.18	**.05**	**.07**	.13	.16	.43	.68	.16	.4	.62	**.05**	**.08**	.17
		∞	.01	0	0	.01	0	0	.04	.01	0	0	0	0	0	0	0	.04	0	0
Aggregate-based	50	70	.04	.04	.04	.04	.02	.01	**.05**	**.05**	**.03**	.03	.02	.01	.02	0	0	**.05**	**.03**	**.03**
		∞	.04	.03	.02	.02	0	0	.05	.03	.01	.01	0	0	0	0	0	.04	.01	.01
	60	50	.06	.06	.05	.06	.09	.12	**.05**	**.05**	**.06**	.06	.07	.1	.08	.16	.31	**.05**	**.06**	**.07**
		70	.05	.05	.04	.05	.03	.02	**.04**	**.05**	**.04**	.04	.03	.03	.03	.02	.01	**.05**	**.04**	**.04**
		∞	.05	.03	.02	.02	0	0	.04	.03	.01	.01	0	0	0	0	0	.04	.02	.01
	70	50	.06	.06	.06	.07	.12	.2	**.06**	**.05**	**.07**	.07	.1	.16	.11	.31	.63	**.05**	**.07**	**.07**
		∞	.05	.03	.03	.02	0	0	.05	.03	.01	.02	0	0	0	0	0	.04	.02	.01

From Table 4, it is seen that for distance-based metrics, only K function attains acceptable Type I error rates under both n_1 and n_2 for both particle-based and aggregate-based centroid patterns. The dispersion metrics based on the centroids of aggregates are slightly more robust than those based on the centroids of nanoparticles.

Table 4. Type I error rates for distance-based methods.

	h_0	h	$n = n_1 = 423$						$n = n_2 = 1409$					
			K		F		G		K		F		G	
			T_1	T_2	T_1	T_2	T_1	T_2	T_1	T_2	T_1	T_2	T_1	T_2
Particle-based	50	70	**.04**	**.04**	.09	.01	.24	.01	**.04**	**.02**	.96	0	.99	0
		∞	.03	.01	.77	0	0	0	.07	0	0	0	0	0
	60	50	**.06**	**.06**	.08	.11	.14	.19	**.05**	**.07**	.6	.7	.72	.79
		70	**.04**	**.05**	.05	.03	.08	.02	**.04**	**.03**	.34	0	.4	0
		∞	.03	.02	.61	0	.99	0	.06	0	0	0	0	0
	70	50	**.07**	**.07**	.12	.17	.27	.36	**.08**	**.1**	.97	.98	.99	0
		∞	.03	.02	.49	0	.94	0	.05	0	0	0	0	0
Aggregate-based	50	70	**.04**	**.04**	.09	.01	.09	.18	**.04**	**.04**	.88	0	.75	.85
		∞	.03	.03	.92	0	.62	.77	.01	.02	0	0	0	0
	60	50	**.06**	**.05**	.11	.14	.05	.04	**.06**	**.06**	.46	.56	.23	0
		70	**.05**	**.05**	.04	.02	.07	.12	**.05**	**.05**	.27	0	.23	.36
		∞	.04	.04	.79	0	.48	.65	.02	.02	0	0	0	0
	70	50	**.06**	**.06**	.18	.24	.08	.02	**.07**	**.07**	.9	.94	.61	0
		∞	.04	.04	.65	0	.38	.55	.02	.02	0	0	0	0

From Table 5, it is seen that the number of aggregates is very sensitive to the assumption of specimen thickness, and thus may not be a qualified dispersion measure when the exact specimen thickness is unavailable. It is imaginable that if the number of aggregates is not robust, the area distribution of aggregates is also not robust. Thus, the dispersion measures based on the unreinforced domains of the polymer [24-28], which are closely related to the inter-aggregate distance, may be even more sensitive.

Table 5. Type I error rates for the number of aggregates

h_0	50			60			70		
h	60	70	∞	50	70	∞	50	60	∞
$n= n_1$	.01	0	0	.25	.01	0	.47	.18	0

$n = n_2$	0	0	0	.63	0	0	.97	.44	0

In Tables 3~5, the results under $h = \infty$ correspond to the performance of the dispersion metrics when a Poisson process is used, in which the actual h_0 ranges from 50nm to 70nm. The resulted Type I error rates under the Poisson process model largely deviate from the nominal level of 0.05. Note that sometimes Type I error rates for using the Poisson process is 0 from the simulation. From the perspective of controlling Type I error rates, this result may argue for the use of the Poisson process. However, it can be expected that in such cases, we have almost no power to detect clustering by using the Poisson process. So the simulation results echo the conclusion from Proposition 2 that a Poisson process can only be seen as the limit of the projected hardcore process when $h \to \infty$. Therefore, it is seriously untenable to use a Poisson process if the true hardcore process does not have a sufficiently large *h*, as is usually the case for real TEM micrographs.

3.3 Detection Power Analysis

Detection power against clustering is an important attribute for evaluating dispersion metrics. The ideal dispersion metric should not only be insensitive to the assumption of *h*, but also sensitive in detecting potential clustering. Further simulation studies are conducted to compare the detection power of the two selected robust dispersion metrics: skewness and K-function. Through simulations, it is possible to find out the performance of the dispersion metrics based on the unobservable 3D point process in $\mathcal{H}$ as compared with their observable counterparts in *W*. So the power analysis also partly answers the question whether the selected 2D dispersion metrics are capable of representing the actual 3D dispersion of nanocomposites. Detailed settings of this simulation are given below:

- w=l=1067nm; r=10.5nm; h=60nm;
- Number of nanoparticles (n): $n_1(\pm 10\% n_1)$, n_2 $(\pm 10\% n_2)$;
- Ratio of intensities between the interior and the exterior of the cluster (R): 2, 3, 4;
- Duplicates of simulation under each setting: 10000.
- Dispersion metrics: skewness and K-function (T_1 and T_2) based on centroids of 3D particles (3p), and centroids of 2D particles (2p) or aggregates (2a)

For the simulation, we assume that each cluster has an ellipsoidal shape in 3D. The center of the ellipsoid is randomly drawn from $\mathcal{H}$ under the constraint that the ellipsoid is completely within $\mathcal{H}$. The semi-axes of the ellipsoid are fixed at one fourth of each dimension of $\mathcal{H}$. The ratio of intensities R between the interior and the exterior of the ellipsoidal cluster is calculated as

$$\boldsymbol{R} = \frac{\boldsymbol{n}_{in} / \boldsymbol{V}_{in}}{\boldsymbol{n}_{ex} / \boldsymbol{V}_{ex}},$$

in which $\boldsymbol{n}_{in}$ and $\boldsymbol{V}_{in}$ denote the number of nanoparticles and the volume in the interior of the ellipsoidal cluster, $\boldsymbol{n}_{ex}$ and $\boldsymbol{V}_{ex}$ denote the number of nanoparticles and the volume in the exterior of the ellipsoidal cluster. Since $\boldsymbol{V}_{in}$, $\boldsymbol{V}_{ex}$ and $\boldsymbol{n} = \boldsymbol{n}_{in} + \boldsymbol{n}_{ex}$ are determined *a prior*, $\boldsymbol{n}_{in}(\boldsymbol{n}_{ex})$ can be uniquely determined for each fixed R. Simulation of the clustering patterns can be conducted by sequentially put $\boldsymbol{n}_{in}$ nanoparticles in the interior and $\boldsymbol{n}_{ex}$ nanoparticles in the exterior of the ellipsoidal cluster respectively under the hardcore constraint.

Figure 3 presents a few simulated point patterns after projecting onto 2D (with the 2D projection of the ellipsoidal cluster represented by circle in Fig. 3). Since the cylinder whose 2D projection coincides with the area enclosed by the circle encompasses regions other than the ellipsoid, the degree of clustering within the circle is diluted to some degree as compared

with that in 3D. It is seen from Fig. 3 that when R=2, it is hard to discern clustering by our naked eyes.

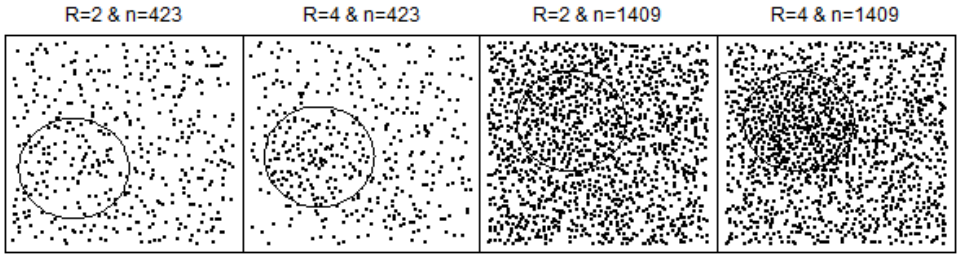

Figure 3. Point patterns with clustering.

For the skewness metric based on the centroids of 3D particles, the h dimension is equally divided into two parts, because the radius of the nanoparticles is not very small as compared with h. As a result, the total number of quadrats is $k=S\times S\times 2$.

For the power analysis, it is desirable to know how to combine multiple available TEM micrographs to provide better detection of clustering. If the point processes generated from m micrographs would follow the same null hypothesis distribution, a simple combining rule can be generated by using some summary statistics (e.g., maximum or mean) of m micrographs as the test statistic. In reality, however, it is likely that micrographs taken at different locations of the specimen contain different number of nanoparticles even if we could assume the same h for different micrographs. Thus, the null hypothesis distribution of the dispersion metrics may vary from micrograph to micrograph when they are taken from the same TEM specimen at different locations. Consequently, the dispersion metrics calculated from multiple micrographs cannot be directly combined.

In order to combine multiple micrographs with the consideration of different number of nanoparticles at different locations of a TEM specimen, we propose to standardize the dispersion metrics so that those micrographs within a TEM specimen would follow similar

null hypothesis distributions. The skewness metric can be both positive and negative and the shape of the distribution is roughly symmetric, so its standardization is achieved by subtracting the sample mean and then dividing by the sample standard deviation. Differently, the K-function metrics must be non-negative and the distribution is right-skewed. So its standardization is done by dividing its sample mean. Our simulation studies show that after standardization, the null distributions of dispersion metrics (skewness and K function) calculated from multiple micrographs of different number of nanoparticles are very similar to each other. Therefore, the test statistics will be constructed by combining multiple micrographs using the standardized metrics instead of the original metrics. Similarly, this standardization can also be used for comparing different samples with possibly different numbers of nanoparticles or specimen thickness.

In practice, since it is hard to known *a priori* the number of nanoparticles in a TEM micrograph, we take a simplified simulation approach in the hope of elucidating the procedures of the power analysis based on multiple micrographs. For each content of nanoparticles (3% or 10%) with an expected number of nanoparticles n (=n_1 or n_2), the number of nanoparticles in each of m (m ranges from 1 to 15) micrographs is randomly set as $n\times 90\%$, n and $n\times 110\%$ with equal probabilities. Under the Poisson model, the number of particles in a micrograph follows a Poisson distribution with n as the expectation. The probability that the number of particles is within 10% of n is about 0.96 for n_1 and almost one for n_2. Under the hardcore process, the variability for the number of particles is even smaller. So a range of 10% covers the possible number of nanoparticles well under the hardcore process with a fixed content of nanoparticles for micrographs taken from the same

original specimen. Then the mean of the standardized dispersion metrics from all m micrographs is used as the test statistic. The results of the power analysis are summarized in Table 6. For skewness, only the results for S=5 are shown, since the case of S=5 has the largest power in all scenarios.

It can be seen from Table 6 that for SK, the metric based on the centroids of 3D particles has the largest power. For K-function, both T_1 and T_2 are the most powerful based on the centroids of 2D particles. The K-function metrics are uniformly more powerful than SK across all ratios of intensities. Within the K-function family, the one-sided test is more powerful than the two-sided test. The performance of the one-sided K-function metric T_2 based on the centroids of 2D particles is superior, which is shown by a power of 80% or more for different number of nanoparticles when the ratio of intensities is moderately large (R=3 or 4) or when multiple images can be combined (e.g., R=2, $n = n_1(\pm 10\% n_1)$, m=5). Although K-function based on the centroids of 2D aggregates does not perform as well as K-function based on the centroids of 2D particles, its power is also quite satisfactory, only except for the case of $n = n_2(\pm 10\% n_2)$. With an increased ratio of intensities or an increased number of combined images, all dispersion metrics become more powerful, except for the case of $n = n_2(\pm 10\% n_2)$ using SK based on the centroids of 2D aggregates. This exception is consistent with our intuition. When a cluster consists of a large number of particles (e.g., under n_2), more particles may belong to the same aggregate, thus resulting in fewer aggregates.

To further clarify this point, the mean ratios of intensities (RoI) between the interior and the exterior of the circle projected from the ellipsoidal cluster for nanoparticles (Fig. 4a)

and for aggregates (Fig. 4b) are plotted against varying numbers of nanoparticles at different levels of *R*. The number of nanoparticles is calculated according to the expected number of nanoparticles with a nanoparticle content ranging from 2% to 15% under a thickness of 60nm. From Fig. 4a, it is seen that the RoI for nanoparticles are above one everywhere for each choice of *R*, which shows that clustering nanoparticles in 3D can always be translated into clustering nanoparticles in the projected 2D micrographs. So dispersion metrics based on the centroids of 2D nanoparticles work well in distinguishing clustering patterns from a null hypothesis of hardcore process. The curves for nanoparticles from different *R* do not cross and the curve with the larger *R* is always above, so the power of 2D particle-based dispersion metrics improves with increasing *R*. In contrast, from Fig. 4b, the RoI for aggregates can be below one when nanoparticle content is large (e.g., 12% or more). In addition, the curves for different *R* cross at around a content of 10%, so increasing *R* does not necessarily signify more severe clustering of aggregates in 2D. At a content of 10% nanoparticles, the corresponding RoIs for all levels of *R* are close to one, which shows no substantial difference of the RoI for aggregates among the null hypothesis hardcore process and the three clustering cases with different *R* levels. This explains why the skewness metric based on the centroids of 2D aggregates at $n = n_2(\pm 10\% n_2)$ only attains a power around the nominal Type I error rate of 0.05 at all levels of *R*.

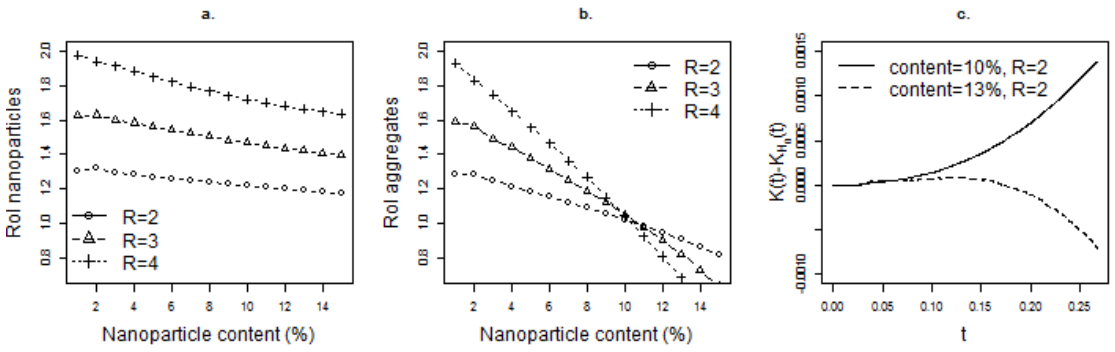

Figure 4.a. Mean RoI for nanoparticles. b. Mean RoI for aggregates. c. Difference between the K-function curve and its reference curve under the hardcore process at a content of 10% and 13% when *R*=2.

For K-function, the same effect also applies when $n = n_2(\pm 10\% n_2)$, but not as severe. The K-function curve still has a small positive distance from the null hypothesis curve (the difference of the two curves at a content of 10% is shown in solid in Fig. 4c), so the power can be enhanced by combining multiple images. In fact, our simulation studies indicate that the power of the one-sided K-function metric based on centroids of 2D aggregates can reach 80% when the ratio of intensities is relatively large (e.g., *R*=3 or 4) and/or when a large number of micrographs can be combined (e.g., *m*>10). For a content of 12% or more, the K-function curve may lie mostly below the null hypothesis curve (the difference of two curves at a content of 13% is shown in dash in Fig. 4c). In this case, the one-sided test statistics T_2 may lose power. Instead, the two-sided statistics T_1 may be a more reasonable choice. Aside from assuming a single ellipsoidal cluster as the clustering pattern, multiple ellipsoidal clusters have also been considered. The conclusions are similar to the single cluster case, so results are omitted here.

Table 6. Power of the skewness and the K function metrics.

R	m	$n_1(\pm 10\% n_1)$									$n_2(\pm 10\% n_2)$								
		SK			T_1			T_2			SK			T_1			T_2		
		3p	2p	2a	3p	2p	2a	3p	2p	2a	3p	2p	2a	3p	2p	2a	3p	2p	2a

2	1	.14	.09	.08	.2	.32	.26	.34	.4	.33	.51	.23	.05	.58	.74	.1	.69	**.83**	.14
	5	.33	.17	.13	.46	.72	.59	.79	**.85**	.74	**.95**	.68	.05	**.97**	**1**	.15	**.99**	**1**	.27
	10	.5	.27	.17	.69	**.92**	**.82**	**.96**	**.98**	**.94**	**1**	**.9**	.05	**1**	**1**	.2	**1**	**1**	.43
	15	.65	.35	.21	**.82**	**.97**	**.91**	**.99**	**1**	**.99**	**1**	**.97**	.05	**1**	**1**	.25	**1**	**1**	.55
3	1	.59	.33	.25	.5	**.9**	**.8**	.63	**.94**	**.85**	**.94**	**.89**	.06	**.86**	**1**	.16	**.9**	**1**	.22
	3	**.91**	.69	.5	**.82**	**1**	**.99**	**.92**	**1**	**.99**	**1**	**1**	.05	**.99**	**1**	.25	**1**	**1**	.36
	5	**.98**	**.88**	.68	**.94**	**1**	**1**	**.98**	**1**	**1**	**1**	**1**	.05	**1**	**1**	.33	**1**	**1**	.48
4	1	**.86**	.68	.51	.65	**1**	**.99**	.75	**1**	**1**	**1**	**1**	.05	**.93**	**1**	.17	**.95**	**1**	.23
	2	**.98**	**.93**	.78	**.86**	**1**	**1**	**.93**	**1**	**1**	**1**	**1**	.04	**.99**	**1**	.24	**1**	**1**	.32
	3	**1**	**.99**	**.91**	**.95**	**1**	**1**	**.98**	**1**	**1**	**1**	**1**	.04	**1**	**1**	.29	**1**	**1**	.39

3.4 Summary of Analysis Procedures

The proposed analysis procedures for detecting possible clustering in TEM micrographs can be summarized in a flowchart as shown in Fig. 5. First, image processing techniques are used to find the number of nanoparticles and the location of the centroids of nanoparticles or aggregates on the micrograph, which will be discussed in Section 4. This information, combined with source information such as w, l, r and a claimed h determines the null hypothesis based on the projected hardcore process. Second, if h is not accurately known, the robust dispersion metrics should be selected. Third, the number of available images determines whether to standardize and combine dispersion metrics from multiple images. Fourth, the dispersion metrics from the real images and their distributions under the null hypothesis of a projected hardcore process are calculated. Finally, a formal statistical hypothesis test can be conducted by comparing the observed test statistic with its distribution under the null hypothesis.

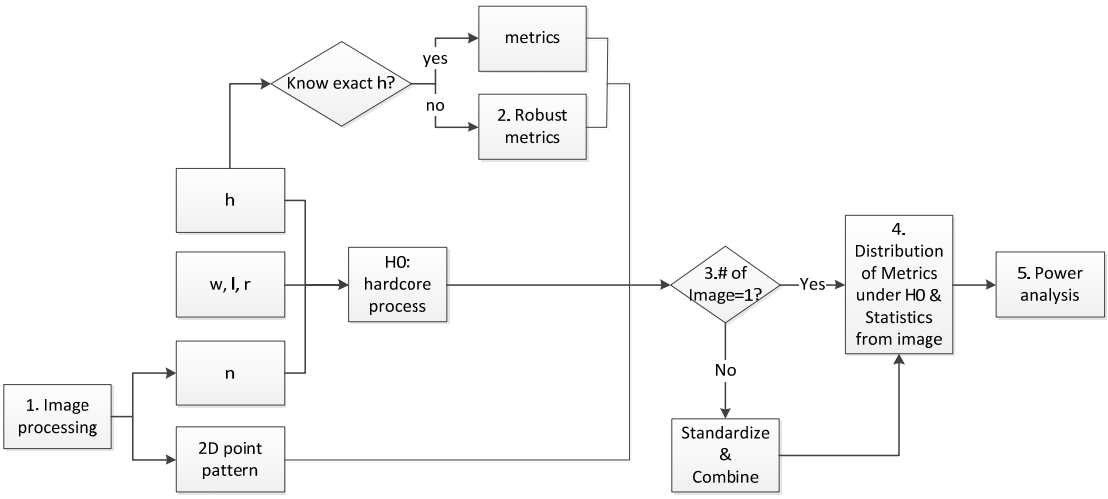

Figure 5. Flowchart for the proposed analysis procedures.

4 Case Study

4.1 Materials and TEM preparation

In this paper, we evaluate the dispersion level of sol-gel-formed silica nanoparticles in bisphenol-F epoxy resin, a polymer nanocomposite that has superior wear-resistant and mechanical properties. Nanocomposite specimen with silica contents at 3% and 10% are cut and prepared into ultra-thin specimens using ultramicrotome. Then silica dispersion is examined by TEM (FEI Tecnai G2 F20 UT) under a magnification factor of 19000 times (i.e., w=l=1067nm). At the content of 3%, one micrograph is taken and the thickness of the specimen is around 60nm. At the content of 10%, three micrographs are taken and the specimen thickness is around 50nm. The average diameter of the nanoparticles is known to be 21nm, which is used as the constant diameter of nanoparticles for the analysis. Figure 6 shows the TEM micrographs under investigation. There are 1024×1024 pixels on each micrograph and each pixel has a grayscale of 0 (black) to 255 (white).

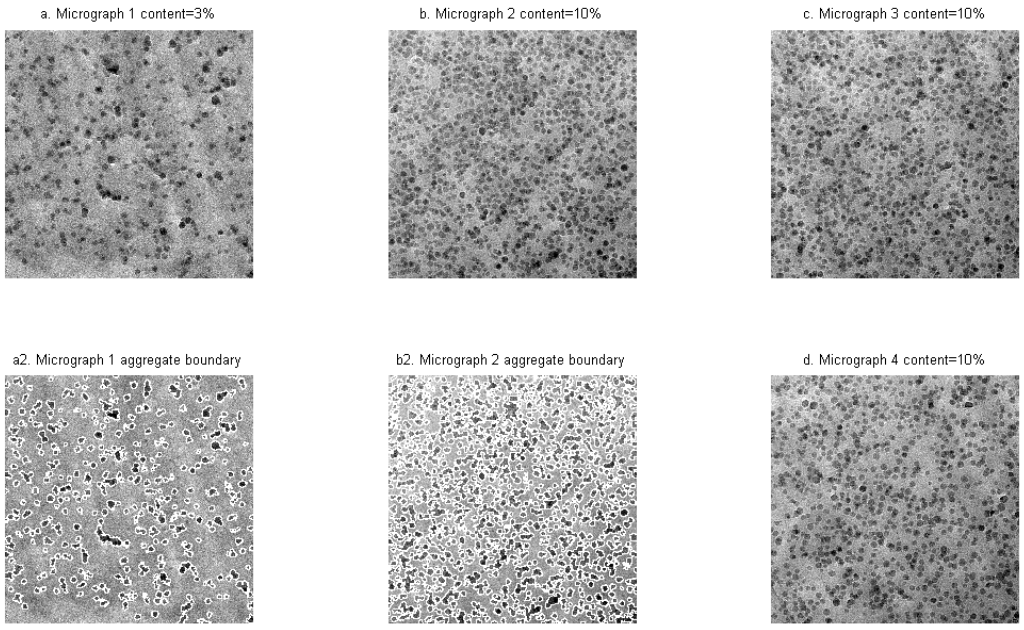

Figure 6. Real TEM micrographs and aggregate boundary detection.

4.2 Image processing

TEM micrographs are digital images that do not provide direct quantitative information. Thus, image processing techniques have to be first applied. Image analysis of TEM micrographs has been studied for metallic nanoparticles [36-39] whose contrast with the polymer background is relatively sharp or for images with no systematic bias on any particular region [40]. However, the observed TEM micrographs have relatively low contrast between the silica nanoparticles and the epoxy background and the bottom right corner of some micrographs is systematically darker than the rest of the regions (see Fig. 6b, 6c, 6d). As a result, a specially designed image processing algorithm is used to binarize the micrograph into white (background) and black (nanoparticle), which we call the "adaptive Gaussian mixture (AGM) algorithm" [41]. The AGM algorithm finds the number of and the positions of the centroids of aggregates in a TEM micrograph. Furthermore, aggregate-based dispersion metrics are relatively more robust when exact information of the specimen thickness is not

available. Therefore we only use aggregate-based dispersion metrics to illustrate the implementation of the proposed procedures. Aside from aggregate information, the number of nanoparticles also has to be obtained from image processing to simulate the projected hardcore process. To this end, the iterative voting method (IVM) [42] is used.

4.3 Results

Following the procedures in Fig. 5, four micrographs are analyzed. Table 8 provides some basic information as well as the p-values obtained from the hypothesis tests for detecting clustering using the skewness metric and the K-function metrics.

Table 8. Analysis results of four micrographs.

Micrograph	# of nanoparticles	# of aggregates	p-value		
			SK	T_1	T_2
1	454	286	0.31	**0.004**	**0.002**
2	1181	508	0.95	**0**	0.97
3	1145	555	0.96	**0.02**	0.98
4	1050	566	0.27	**0.03**	0.96
p-value from combined test statistics			0.95	**2E-4**	1

For micrograph 1, the skewness metric cannot detect significant clustering, but both K-function metrics declare a highly significant difference from the null hypothesis. For micrograph 2, 3 and 4, only the two-sided K-function metric suggests a difference from the null hypothesis. But this phenomenon may happen either when the 3D point process is more regular than a hardcore process or when the clustering of nanoparticles generates fewer aggregates. A closer look at those three micrographs suggests evidence of clustering. First, the number of aggregates in those micrographs is far below the reasonable range. For example, the 5^{th} percentile of the number of aggregates for a Poisson process with 1145 nanoparticles is 518. This number should be larger for a hardcore process with a limited *h*.

However, micrograph 2 has only 508 aggregates with more than 1145 nanoparticles. So, there is evidence that clustering results in fewer aggregates. Second, the point process generated from the centroids of nanoparticles using the IVM method [42], though subject to more errors in image processing, also indicates statistical significance in testing clustering using the one-sided K-function metric when combining three micrographs ($p=0.03$). The results of the analysis show that a random dispersion of nanoparticles is not achieved within the polymer matrix. Whether and how the clustering of nanoparticles affects the properties of the nanocomposites is a question to be investigated in future.

5 Conclusions

In this paper, we propose to use the projection of a 3D hardcore process instead of the Poisson process to model the 3D random distribution of hard nanoparticles in polymer nanocomposites shown on a TEM micrograph. The thickness of the thin specimen h under imaging is identified as an important factor to influence how different a hardcore process and a Poisson process are. Since it is generally hard in practice to accurately measure thickness, the impact of a misspecification of h is investigated through simulations, based on which robust dispersion metrics using skewness of quadrat counts and the squared deviation of the K-function curves are recommended. Further power analysis of these dispersion metrics show that the K-function related metrics have relatively better power to detect clustering, especially when multiple micrographs are available to be combined in the analysis.

The proposed hardcore model is under the assumption of a constant size for nanoparticles. This model is a more realistic simplification and approximation for nanoparticle dispersion in 3D than the existing methods using the Poisson process. It is now

well known that a uniform particle size is a key to enhance novel properties and high performance of nanoparticles [43]. Especially, monodisperse nanoparticles with a size variation of less than 5% show unique properties and better performance as compared with the corresponding polydisperse nanoparticles [43]. Nowadays, with the advancement of nanotechnology, it is not uncommon to synthesize nanoparticle with its size's standard deviation less than 10% [44]. We conducted more simulations with nanoparticle radius following a normal distribution with mean r and standard deviation σ_r equal to $0.1r$. The simulation results with the radius distribution of N(10.5,0.105) indicate that the Type I errors are close to the nominal level of 0.05 under the assumption of a constant nanoparticle radius equal to 10.5nm. Therefore, in practical situations with a small random variation of nanoparticle size ($\sigma_r \leq 0.1r$), our analysis based on the assumption of a constant nanoparticle size can still provide reliable inferences. For cases in which nanoparticles may have a wide range of sizes, a marked point process with each nanoparticle marked with its radius may deserve further investigation.

A quantitative index for nanoparticle dispersion is essentially needed to build a quantitative relationship between dispersion and process parameters or between dispersion and nanocomposite properties. The former facilitates optimization of the process parameters, and the latter provides rational choice of the index as a reliable surrogate for destructive property testing. Establishment of these relationships completes the loop of dispersion analysis and is the next thing we shall pursue.

Appendix.

Proof of Proposition 2.1.

Let $\{\boldsymbol{x_i}, i = 1, \dots, n\}$ denote random variables that are uniformly distributed in $\mathcal{H}$, let d=2r be the diameter of the nanoparticles and let $A_{ij} = \{\|\boldsymbol{x_i} - \boldsymbol{x_j}\| \le d, \boldsymbol{x_i}, \boldsymbol{x_j} \in \mathcal{H}, 1 \le i, j \le n\}$, then it is easy to see that

$$\alpha = 1 - P\left(\bigcup_{i \neq j} A_{ij}\right).$$

From the Bonferroni inequality,

$$\sum_{i \neq j} \mathrm{P}(A_{ij}) - \sum_{(i,j) \neq (k.l)} \mathrm{P}(A_{ij} \cap A_{kl}) + \sum_{(i,j) \neq (k.l) \neq (p,q)} \mathrm{P}(A_{ij} \cap A_{kl} \cap A_{pq}) \ge 1 - \alpha$$

$$\ge \sum_{i \neq j} \mathrm{P}(A_{ij}) - \sum_{(i,j) \neq (k.l)} \mathrm{P}(A_{ij} \cap A_{kl}). \quad (1)$$

So the proof reduces to the calculation of each of the probabilities in (1). The techniques for deriving inequalities for each of the probabilities in (1) are similar, so we only use $\mathrm{P}(A_{ij})$ as an example.

Assume that $\mathcal{H}$ is partitioned into three sub-regions: R1, R2, and R3 (shown in Fig. 7). R1 is the innermost region enclosed by dashed lines. For any point $\boldsymbol{x}$ in R1, a sphere with $\boldsymbol{x}$ as the center and a radius of d does not intersect with the boundary of $\mathcal{H}$. The sub-region R2 is made up of six cuboids, one side for each of which is within one of the six sides of $\mathcal{H}$. For any point $\boldsymbol{x}$ in R2, a sphere with $\boldsymbol{x}$ as the center and a radius of d only intersects one side of $\mathcal{H}$. The rest of the regions comprise R3, which includes the eight corner cubes and the twelve cuboids, one edge of which is within one of the twelve edges of $\mathcal{H}$. For any point $\boldsymbol{x}$ in R3, a sphere with $\boldsymbol{x}$ as the center and a radius of d intersects two or three sides of $\mathcal{H}$.

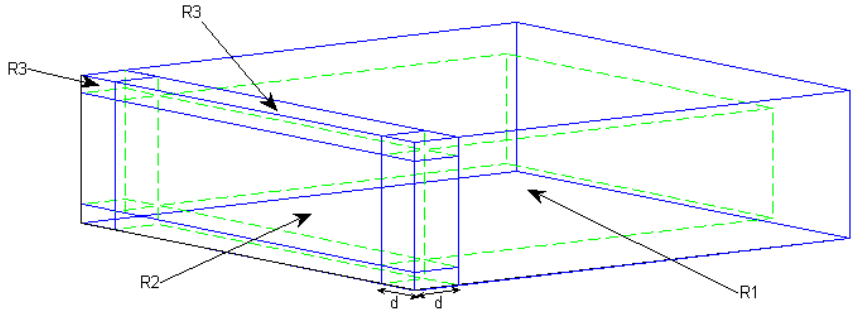

Figure 7. Partition of $\mathcal{H}$.

Let V_1, V_2 and V_3 denote the volume of R1, R2 and R3, where $V_1 = (l - 2d)(w - 2d)(h - 2d), V_2 = 2d\{(w - 2d)(l - 2d) + (w - 2d)(h - 2d) + (l - 2d)(h - 2d)\}$, $V_3 = 8d^3 + 4(w - 2d)d^2 + 4(l - 2d)d^2 + 4(h - 2d)d^2$. $\mathrm{P}(A_{ij})$ can be decomposed into three parts, depending on where $\boldsymbol{x_i}$ is. It is easy to see that $\mathrm{P}(\boldsymbol{x_i} \in R_1, \|\boldsymbol{x_i} - \boldsymbol{x_j}\| \le d) =$

$\frac{V_1}{wlh}\frac{4\pi d^3/3}{wlh} = a_1$ and $0 \le \mathrm{P}\left(\boldsymbol{x_i} \in R_3, \left\|\boldsymbol{x_i} - \boldsymbol{x_j}\right\| \le d\right) \le \frac{V_3}{wlh}\frac{4\pi d^3/3}{wlh} = c_1$. The case in which a point is in $R_{21} = [d, w-d] \times [d, l-d] \times [0, d]$, a subset of R_2 can be derived from the following integral:

$$\mathrm{P}\left(\boldsymbol{x_i} \in R_{21}, \left\|\boldsymbol{x_i} - \boldsymbol{x_j}\right\| \le d\right) = \iiint\limits_{\boldsymbol{x_i} \in R_{21}} \mathrm{d}\boldsymbol{x_i} \iiint\limits_{\|x_i - x_j\| \le d} \mathrm{d}\boldsymbol{x_j} \Big/ (wlh)^2$$

$$= \iint\limits_{\substack{d \le x_{i1} \le w-d \\ d \le x_{i2} \le l-d}} \mathrm{d}x_{i1}\mathrm{d}x_{i2} \int\limits_{0 \le x_{i3} \le d} (\pi d^2 x_{i3} - \frac{\pi x_{i3}^3}{3} + 2\pi d^3/3)\mathrm{d}x_{i3} \Big/ (wlh)^2$$

$$= d(w-2d)(l-2d)(\frac{13\pi d^3}{12}) / (wlh)^2.$$

Summing up all sub-regions of R_2 gives that $\mathrm{P}\left(\boldsymbol{x_i} \in R_2, \left\|\boldsymbol{x_i} - \boldsymbol{x_j}\right\| \le d\right) =$ $\frac{V_2}{wlh}\frac{13\pi d^3/12}{wlh} = b_1$. So $l_1\frac{\pi d^3}{wlh} = a_1 + b_1 \le \mathrm{P}(A_{ij}) = \sum_{s=1}^{3} \mathrm{P}\left(\boldsymbol{x_i} \in R_s, \left\|\boldsymbol{x_i} - \boldsymbol{x_j}\right\| \le d\right) \le a_1 + b_1 + c_1 = u_1\frac{\pi d^3}{wlh}$. Similarly, it can be shown that $l_2(\frac{\pi d^3}{wlh})^2 = a_2 + b_2 \le \mathrm{P}(A_{ij} \cap A_{ik}) \le a_2 + b_2 + c_2 = u_2(\frac{\pi d^3}{wlh})^2, l_3(\frac{\pi d^3}{wlh})^3 = a_3 + b_3 \le \mathrm{P}(A_{ij} \cap A_{ik} \cap A_{iq}) \le a_3 + b_3 + c_3 = u_3(\frac{\pi d^3}{wlh})^3$ and $\mathrm{P}(A_{ij} \cap A_{ik} \cap A_{pj}) \le \frac{(4\pi d^3/3)^2}{(wlh)^2}\mathrm{P}(A_{ij})$, where $a_2 = \frac{V_1}{wlh}\left(\frac{4\pi d^3/3}{wlh}\right)^2, b_2 = \frac{V_2}{wlh}\frac{383(\pi d^3)^2/315}{(wlh)^2}, c_2 = \frac{V_3}{wlh}\left(\frac{4\pi d^3/3}{wlh}\right)^2, a_3 = \frac{V_1}{wlh}\left(\frac{4\pi d^3/3}{wlh}\right)^3, b_3 = \frac{V_2}{wlh}\frac{10621(\pi d^3)^3/7560}{(wlh)^3}$ and $c_3 = \frac{V_3}{wlh}\left(\frac{4\pi d^3/3}{wlh}\right)^3$. From combinatorics theory, it can be shown that $\sum_{\mathrm{i}\neq\mathrm{j}} \mathrm{P}(\mathrm{A_{ij}}) = g_1(n)\mathrm{P}(A_{12}), \sum_{(i,j)\neq(k.l)} \mathrm{P}(A_{ij} \cap A_{kl}) = g_{21}(n)\mathrm{P}^2(A_{12}) + g_{22}(n)\mathrm{P}(A_{12} \cap A_{13}),$

$\sum_{(i,j)\neq(k,l)\neq(p,q)} \mathrm{P}(A_{ij} \cap A_{kl} \cap A_{pq}) = g_{31}(n)\mathrm{P}^3(A_{12}) + g_{32}(n)\mathrm{P}(A_{12})P(A_{12} \cap A_{13}) + g_{33}(n)\mathrm{P}(A_{12} \cap A_{13} \cap A_{14}) + g_{34}(n)\mathrm{P}(A_{12} \cap A_{13} \cap A_{24}) + g_{35}(n)\,\mathrm{P}(A_{12} \cap A_{13} \cap A_{23}),$ where $g_1(n) = \binom{n}{2}, g_{21}(n) = \frac{\binom{n}{2}\binom{n-2}{2}}{2}, g_{22}(n) = \binom{n}{2}(n-2), g_{31}(n) = \binom{n}{2}\binom{n-2}{2}\binom{n-4}{2}/3!,$ $g_{32}(n) = \binom{n}{1}\binom{n-1}{2}\binom{n-3}{2}, g_{33}(n) = \binom{n}{1}\binom{n-1}{3}, g_{34}(n) = 2\binom{n}{2}\binom{n-2}{2}$ and $g_{35}(n) = \binom{n}{3}$.

Summarizing all results, $s_1(n) = 8g_1(n)l_1, s_2(n) = 64(g_{21}(n)u_1^2 + g_{22}(n)u_2), t_1(n) = 8g_1(n)u_1, t_2(\mathrm{n}) = 64(g_{21}(n)l_1^2 + g_{22}(n)l_2 - g_{35}(n)u_2)$, and $t_3(n) = 512(g_{31}(n)u_1^3 + g_{32}(n)u_1u_2 + g_{33}(n)u_3 + 16g_{34}(n)u_1/9)$.

Reference

[1] Ajayan, P., Schadler, L., Braun, P., 2003, Nanocomposite Science and Technology, WILEY-VCH Verlag, GmbH & Co. KGaA, Weinheim, Chap.2.

[2] Ray, S., Okamoto, M., 2003, "Polymer/layered Silicate Nanocomposites: a Review from Preparation to Processing," Progress in Polymer Science **28** (11), pp. 1539-1641.

[3] Paul, D., Robeson, L., 2008, "Polymer Nanotechnology: Nanocomposites," Polymer, **49**, pp. 3187-3204.

[4] Thostensen, E., Li, C., Chou, T., 2005, "Nanocomposites in Context," Composites Science and Technology, **65** (3-4), pp. 491-516.

[5] Njuguna, J., Pielichowski, K., 2004, "Polymer Nanocomposites for Aerospace Applications: Fabrication," Advanced Engineering Materials, **6**(4), pp. 193-203.

[6] West, D., Malhotra, V., 2006, "Rupture of Nanoparticle Agglomerates and Formulation of Al2O3-epoxy Nanocomposites Using Ultrasonic Cavitation Approach: Effects on the Structural and Mechanical Properties," Polymer Engineering & Science, **46**(4), pp. 426-430.

[7] Naous, W., Yu, X., Zhang, Q., Naito, K., Kagawa, Y., 2006, "Morphology, Tensile Properties, and Fracture Toughness of Epoxy/Al2O3 Nanocomposites," Journal of Polymer Science Part B – Polymer Physics, **44**(10), pp. 1466-1473.

[8] Wetzel, B., Rosso, P., Haupert, F., Friedrich, K., 2006, "Epoxy Nanocomposites – Fracture and Toughening Mechanisms," Engineering Fracturing Mechanics, **73**(16), pp. 2375-2398.

[9] Zuiderduin, W., Westzaan, C., Huetink, J., Gaymans, R, 2003, "Toughening of Polypropylene with Calcium Carbonate Particles," Polymer, **44**, pp. 261-275.

[10] Li, Z., Okamoto, K, Ohki, Y., Tanaka, T., 2011, "The Role of Nano and Micro Particles on Particle Discharge and Breakdown Strength in Epoxy Composites," IEEE Transactions on Dielectrics and Electrical Insulation, **18**(3), pp. 675-681.

[11] Zhang, H., Zhang, H., Tang, L., Zhang, Z., Gu, L., Xu, Y., Eger, C., 2010, "Wear-resistant and Transparent Acrylate-based Coating with Highly Filled Nanosilica Particles," Tribology International, **43**(1-2), pp. 83-91.

[12] Khare, H., Burris, D., 2010, "A Quantitative Method for Measuring Nanocomposite Dispersion," Polymer, **51**, pp. 719-729.

[13] Fultz, B., Howe, J., 2013, Transmission Electron Microscopy and Diffractometry of Materials, Springer-Verlag, Berlin Heidelberg, Chap 5.

[14] Cressie, N., 1993, Statistics for Spatial Data, Wiley-Interscience, New York, NY, Chap. 8.

[15] Diggle, P., 2003, Statistical Analysis of Spatial Point Patterns, Arnold, London, Chap. 2.

[16] Illian J, Penttinen A, Stoyan H, Stoyan D (2008). Statistical Analysis and Modeling of Spatial Point Patterns. Wiley-Interscience, Chichester, UK, Chap. 1.

[17] Kim, D., Lee, J., Barry, C., Mead, J., 2007, "Microscopic Measurement of the Degree of Mixing for Nanoparticles in Polymer Nanocomposites by TEM Images," Microscopy Research and Technique, **70**, pp. 539-546.

[18] Hui, L., Smith, R., Wang, X., Nelson, J., Schadler, L., 2008, "Quantification of Particulate Mixing in Nanocomposites," Annual Report Conference on Electrical

Insulation Dielectric Phenomena, pp. 317-320.

[19] Liu, J., Gao, Y., Cao, D., Zhang, L., Guo, Z., 2011, "Nanoparticle Dispersion and Aggregation in Polymer Nanocomposites: Insights from Molecular Dynamics Simulation," Langmuir, **27**, pp. 7926-7933.

[20] Duyckaerts, C., Godefroy, G., Hauw, J., 1994, "Evaluation of Neuronal Numerical Density by Dirichlet Tessellation," Journal of Neuroscience Methods, **51**, pp. 47-69.

[21] Myles, J., Flenley, E., Fieller, N., Atkinson, H., Jones, H., 1995, "Statistical Tests for Clustering of Second Phases in Composite Materials," Philosophical Magazine A, **72**(2), pp. 515-528.

[22] Tong, L., Wang, C., Chen, D., 2007, "Development of a New Cluster Index for Wafer Defects," International Journal of Advanced Manufacturing Technology, **31**(7-8), pp. 705-715.

[23] Zhou, Q., Zeng, L., DeCicco, M., Li, X., Zhou, S., 2012, "A Comparative Study on Clustering Indices for Distribution of Nanoparticles in Metal Matrix Nanocomposites," *CIRP* Journal of Manufacturing Science and Technology, **5**(4), pp.348-356.

[24] Basu, S., Tewari, A., Fasulo, P., Rodgers, W., 2007, "Transmission Electron Microscopy Based Direct Mathematical Quantifiers for Dispersion in Nanocomposites," Applied Physics Letters, **91**(5), pp. 053105-053105-3.

[25] Hamming, L., Qiao, R., Messersmith, P., Brinson, L., 2009, "Effects of Dispersion and Interfacial Modification on the Macroscale Properties of TiO_2 Polymer-matrix Nanocomposites," Composites Science and Technology, **69**, pp.1880-1886.

[26] Xie, S., Harkin-Jones, E., Shen, Y., Hornsby, P., McAfee, M., McNally, T., Patel, R., Benkreira, H., Coates, P., 2010, "Quantitative Characterization of Clay Dispersion in Polypropylene-clay Nanocomposites by Combined Transmission Electron Microscopy and Optical Microscopy," Materials Letters, **64**(2), pp. 185-188.

[27] Luo, Z., Koo, J., 2007, "Quantifying the Dispersion of Mixture Microstructures," Journal of Microscopy, **225**(2), pp. 118-125.

[28] Khare, H., Burris, D., 2010, "A Quantitative Method for Measuring Nanocomposite Dispersion," Polymer, **51**, pp. 719-729.

[29] Guise, O., Strom, C., 2011, "Quantifying Dispersion in Polymer Systems by Combining Image Analysis and Statistical Analysis," Microscopy and Microanalysis, **17**(S2), pp. 1472-1473.

[30] Bray, D., Gilmour, S., Guild, F., Hsieh, T., Masania, K., Taylor, A., 2011, "Quantifying Nanoparticle Dispersion: Application of the Delaunay Network for Objective Analysis of Sample Micrographs," Journal of Materials Science, **46**(19), pp. 6437-6452.

[31] Basu, S., Fasulo, P., Rodgers, W., 2011, "Stereology-based Quantitative Characterization of Dispersion from TEM Micrographs of Polymer-clay Nanocomposites," Journal of Applied Polymer Science, **119**(1), pp. 396-411.

[32] Fornes, T., Paul, D., 2003, "Modeling Properties of Nylon6/clay Nanocomposites Using Composite Theories," Polymer, **44**, pp. 4993-5013.

[33] Dennis, H., Hunter, D., Chang, D., Kim, S., White, J., Cho, J., Paul, D., 2001, "Effect of Melt Processing Conditions on the Extent of Exfoliation in Organoclay-based Nanocomposites," Polymer, **42**, pp. 9513-9522.

[34] Ripley, B., 1979, "Algorithm AS 137: Simulating Spatial Patterns: Dependent Samples

from a Multivariate Density," Journal of the Royal Statistical Society, Series C (Applied Statistics), **28**(1), pp. 109-112.

[35] Curtis, J., McIntosh, R., 1950, "The Interrelations of Certain Analytic and Synthetic Phytosociological Characters," Ecology, **31**, pp. 434-455.

[36] McFarland, A., Van Duyne, R., 2003, "Single Silver Nanoparticles as Real-time Optical Sensors with Zeptomole Sensitivity," Nano letters, **3**(8), pp. 1057-1062.

[37] Glotov, O., 2008, "Image Processing of the Fractal Aggregates Composed of Nanoparticles," Russian Journal of Physical Chemistry A, Focus on Chemistry, **82**(13), pp. 2213-2218.

[38] Chen, L., Ho, C., 2008, "Development of Nanoparticle Shape Measurement and Analysis for Process Characterization of T_iO_2 Nanoparticle Synthesis," Review on Advanced Material Science, **18**(8), pp. 677-684.

[39] Park, C., Huang, J., Huitink, D., Kundu, S., Mallick, B., Liang, H., Ding, Y., 2012, "A Multi-stage, Semi-automated Procedure for Analyzing the Morphology of Nanoparticles," IIE Transactions Special Issue for Quality and Design Issues in Nanomanufacturing Systems, **44**(7), pp. 507-522.

[40] Fisker, R., Carstensen, J., Hansen, M., Bdker, F., Morup, S., 2000, "Estimation of Nanoparticle Size Distributions by Image Analysis," Journal of Nanoparticle Research, **2**(3), pp. 267-277.

[41] Li, X., Jin, J., Huang, D., Yu, D., 2012, "The Adaptive Gaussian Mixture Algorithm on Digital Image Binarization", Technical report, Academy of Mathematics and Systems Science, Chinese Academy of Sciences, Beijing.

[42] Parvin, B., Yang, Q., Han, J., Chang, H., Rydberg, B., Barcellos-hoff, M., 2007, "Iterative Voting for Inference of Structural Saliency and Characterization of Subcellular Events," IEEE Transactions on Image Processing, **16**(3), pp. 615-623.

[43] Cui, H., Feng, Y., Ren, W., Zeng, T., Lv, H., Pan, Y., 2009, "Strategies of Large Scale Synthesis of Monodisperse Nanoparticles," Recent Patents on Nanotechnology, 3, pp.32-41.

[44] Chen, M., Falkner, J., Guo, W., Zhang, J., Sayes, C., Colvin, V., 2005, "Synthesis and Self-organization of Soluble Monodisperse Palladium Nanoclusters," Journal of Colloidal and Interface Science, 287, pp. 146-151.